Oxidation mechanism and kinetics of nuclear-grade FeCrAl alloys in the temperature range of 500–1500 °C in steam

Chaewon Kim[a,b], Chongchong Tang[a], Mirco Grosse[a], Yunhwan Maeng[c], Changheui Jang[b,*], Martin Steinbrueck[a,*]

[a] *Institute for Applied Materials (IAM), Karlsruhe Institute of Technology (KIT), Karlsruhe D-76021, Germany*
[b] *Department of Nuclear and Quantum Engineering, Korea Advanced Institute of Science and Technology (KAIST), Daejeon 34141, Republic of Korea*
[c] *Korea Electric Power Corporation-Engineering & Construction Company ((KEPCO-E&C), Gimcheon 39660, Republic of Korea*

ARTICLE INFO

Keywords:
ATF claddings
Nuclear-grade FeCrAl
High-temperature steam oxidation
Oxidation kinetics

ABSTRACT

The oxidation mechanism and kinetics of two nuclear-grade FeCrAl alloys were investigated in steam up to 1500 °C by transient and isothermal oxidation tests. The slow α-alumina formation kinetics well matched only for the temperature range from 1000 °C to 1300 °C. Below 1000 °C, formation of transient alumina caused faster kinetics. In addition, an excessive Fe-rich oxide formation was observed on the inner surface due to rough surface at 600 °C. Above 1300 °C, convoluted α-alumina was easily spalled and caused faster kinetics. Moreover, the oxide spallation caused Cr and Al depletion and catastrophic oxidation above 1400 °C by the formation of Fe-rich oxide. The catastrophic oxidation caused a liquid phase in Fe-rich oxides, which significantly changed the tube segment geometry.

1. Introduction

Since the Fukushima nuclear accident, worldwide efforts have been made for the development of accident tolerant fuel (ATF) cladding materials to mitigate the excessive hydrogen production from the oxidation of current Zr-alloy claddings [1–5]. Among ATF cladding candidates, Fe-based alloys such as FeCrAl exhibited superior oxidation resistance and good mechanical properties [1]. However, Fe-based cladding materials should have a thinner thickness due to the higher neutron absorption cross-section of Fe and Cr compared to Zr. High Cr and Al contents have benefit for the corrosion and oxidation resistance. However, high Al content makes steels brittle, which makes it difficult to produce thin cladding tubes. High Cr content also makes alloys susceptible to thermal and irradiation embrittlement owing to the accelerated phase decomposition. Thus, Oak Ridge National Laboratory (ORNL) developed nuclear-grade FeCrAl alloys containing lower Cr content compared to commercial Kanthal alloys to mitigate the embrittlement issue [6].

While commercial FeCrAl alloys show slow oxidation kinetics by forming a protective alumina layer in high-temperature steam environments [7,8], nuclear-grade FeCrAl alloys also have superior oxidation resistance in spite of their lower Cr content [6,8]. As the oxidation behavior at higher temperature is critical to estimate hydrogen release during design based accidents (DBA), most studies on high-temperature oxidation behavior were conducted at 1200 °C [8,9]. Nevertheless, the oxidation behavior at lower temperature also plays an important role in the early stage of severe accidents or lower temperature accidents in spent fuel pool (SFP). However, only few results have been reported on the oxidation behavior of nuclear-grade FeCrAl alloys below 1000 °C and above 1300 °C.

Li et al. [10] conducted air oxidation tests at 300 °C to 600 °C using a nuclear-grade FeCrAl alloy, C26M (12Cr-6Al-2Mo). After exposed at 600 °C for 2000 h in air, a very thin Al-rich oxide layer of about 45 nm was formed. Although the oxidation resistance at 600 °C was confirmed for a long time, the test was conducted in air, which is less severe than steam. Recently, higher weight gain for the same alloy, C26M, was reported in steam than in air at 800 °C to 1000 °C [11]. Furthermore, more weight gain was observed at 900 °C than at 1100 °C in steam. This observation is the typical oxidation behavior of alumina-forming alloys, which is caused by the transient alumina formation with faster kinetics than α-alumina [12]. However, most simulations to assess the accident scenarios have used the extrapolated oxidation kinetics of α-alumina at lower oxidation temperatures. Thus, oxidation kinetics can be under-estimated at lower temperatures, where the transient alumina formation is dominant. Therefore, the steam oxidation behavior at lower temperatures for a longer time is needed for more accurate simulation of accident sequences.

* Corresponding authors.
E-mail addresses: chjang@kaist.ac.kr (C. Jang), martin.steinbrueck@kit.edu (M. Steinbrueck).

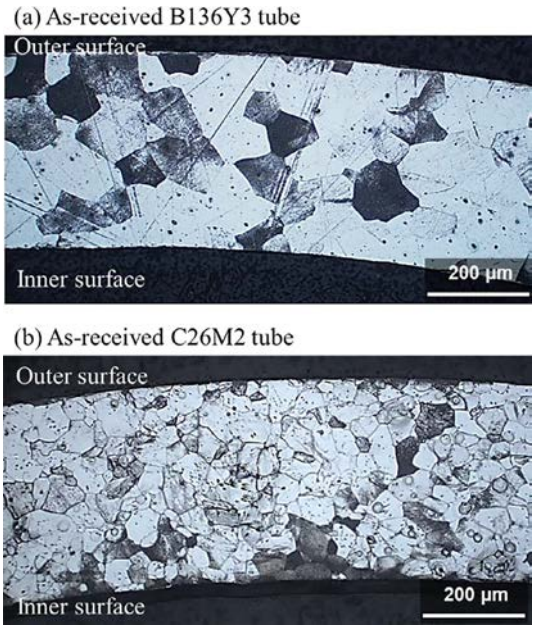

Fig. 1. Cross-sectional optical micrographs of (a) the as-received B136Y3 tube and (b) the as-received C26M2 tube after etching.

Similar to the oxidation behavior at lower temperatures, studies on oxidation behavior at higher temperature above 1300 °C were also rarely found. Dryepondt et al. [13] conducted oxidation tests in steam at 1400 °C and 1450 °C using oxide dispersion strengthened (ODS) Fe-12Cr-5Al alloys. The ODS Fe-12Cr-5Al alloys exhibited a protective alumina at 1400 °C but the protective oxide layer was failed at 1450 °C. Also, the oxidation tests used coupon specimens with the thickness of 2 mm and the alumina failure depended on the specimen thickness and specimen shapes [14]. Therefore, the oxidation kinetics data with prototypical thin tubular specimens is also needed for more accurate simulation of accident sequences.

In this study, nuclear-grade FeCrAl alloys were exposed to steam atmosphere in a wide temperature range to provide the oxidation kinetics information. Transient oxidation tests from 500 °C to 1250 °C and isothermal oxidation tests in temperature range from 600 °C to 1500 °C for 20 h were conducted using two nuclear-grade FeCrAl tubes. After the oxidation tests, oxide layers on the FeCrAl alloys were analyzed and the steam oxidation kinetics is discussed in view of accident scenarios.

2. Materials and experimental methods

Two nuclear-grade FeCrAl alloys, B136Y3 and C26M2, were provided by ORNL in tubular shapes. Both tubes had the same outer diameter (OD) of 9.6 mm; the wall thickness was 0.425 mm and 0.45 mm for B136Y3 and C26M2 tubes, respectively. The details of the tube manufacturing process can be found elsewhere [15]. Fig. 1 shows optical micrographs of two nuclear-grade FeCrAl alloys after etching with solution of glycerin of 45 ml, HNO_3 of 15 ml, and HCl of 30 ml. The grains of two alloys are rather uniformly distributed, while C26M2 tube had smaller grains (30 $\sim$ 70 μm) than B136Y3 tube (80 $\sim$ 130 μm). To compare the transient oxidation behavior in steam, two commercial FeCrAl alloys, APM and APMT in a rod shape, were purchased from Kanthal Sandvik, Sweden. The chemical compositions of all four FeCrAl alloys are listed in Table 1. The chemical compositions of two nuclear-grade FeCrAl alloys were provided by ORNL and those of APM and APMT were analyzed by energy-dispersive X-ray spectroscopy (EDS).

Table 1
Chemical compositions of FeCrAl alloys used in this study.

wt.%	Fe	Cr	Al	Mo	Y	C	Si
APM	Bal	21.13	6.82	–	–	<0.08	<0.7
APMT		21.52	5.73	2.15	–	<0.08	<0.7
B136Y3		12.97	6.19	–	0.03	<0.01	–
C26M2		11.87	6.22	1.98	0.03	<0.01	0.2

For oxidation tests, two nuclear-grade FeCrAl tubes were cut to specimens with length of 10 mm for a simultaneous thermal analyzer system (STA 449 F3, NETZSCH) and 20 mm for a horizontal tube furnace oxidation facility (named BOX facility), respectively. The commercial FeCrAl alloys were fabricated to disk-type specimens with a thickness of 2 mm and a diameter of 10 mm for APM and 8 mm for APMT, respectively.

Two steam oxidation facilities, STA 449 F3 and BOX, were used in this study. The STA 449 F3 is only used in the thermogravimetric (TG) mode with a water vapor furnace capable of almost 100% steam atmosphere up to 1250 °C (named STA facility). A ceramic ring and Pt meshed sample holder were utilized for tubular specimens, and a ceramic crown structure was used for disk-type specimens to avoid undesired interaction between specimens and sample holders, and to provide access of the oxidizing atmosphere to almost whole surface. For transient oxidation tests, the furnace was heated to 500 °C in Ar gas with a flow rate of 50 ml/min and kept for 10 min at this temperature to stabilize the temperature in the test zone. Steam was injected to the test zone with a flow rate of 2 g/h, and temperature was increased up to 1250 °C with a heating rate of 1 °C/min. Ar gas comes and leaves the furnace in the lower part, 100% steam atmosphere is expected at the sample location [16]. After temperature reached 1250 °C, the temperature was maintained for 10 min. Then, steam injection was stopped and temperature was decreased with a rate of 50 °C/min down to room temperature. For isothermal oxidation tests, Ar gas was provided with the same flow rate of 50 ml/min and the furnace was heated up to target isothermal temperatures. After the stabilization for 10 min, steam was injected to the test zone with a flow rate of 2 g/h. Temperature was kept for 20 h and the furnace was cooled down in flowing Ar atmosphere.

The BOX facility with higher temperature capability was utilized to evaluate the oxidation behavior at the temperature above 1250 °C. For the transient oxidation tests, the specimens were loaded on alumina boats with alumina cylinders to minimize the contact of specimens and the boats. Then, Ar gas was supplied into the test zone with a rate of 20 l/h and the furnace was heated up to 500 °C. To stabilize the temperature in the test zone, temperature was maintained for 30 min. Then, steam was injected with a rate of 20 g/h, which results in approximately 55% steam concentration, and the temperature was increased up to 1500 °C with a heating rate of 1 °C/min. When the temperature reached 1500 °C, the steam injection was stopped and the furnace was cooled down with a cooling rate of 10 °C/min. For isothermal oxidation tests, the specimens were heated in 20 l/h Ar gas flow to target isothermal temperatures. When the target temperature has reached, the temperature was maintained for 30 min for the stabilization. Then, steam was injected with a flow rate of 20 g/h and the isothermal test temperature was kept for 20 h. The details of the test schedules for the transient and isothermal oxidation tests in the STA and BOX facilities are described in Fig. 2. Steam was provided to the test zone during the period marked in dashed and blue line in the figure.

Although the BOX facility is not equipped with an analytical balance, high-resolution gas mass spectrometer (IPI GAM3000) is connected to the gas outlet of BOX facility to detect H_2 and Ar release during oxidation tests. H_2 and Ar release rates were recorded

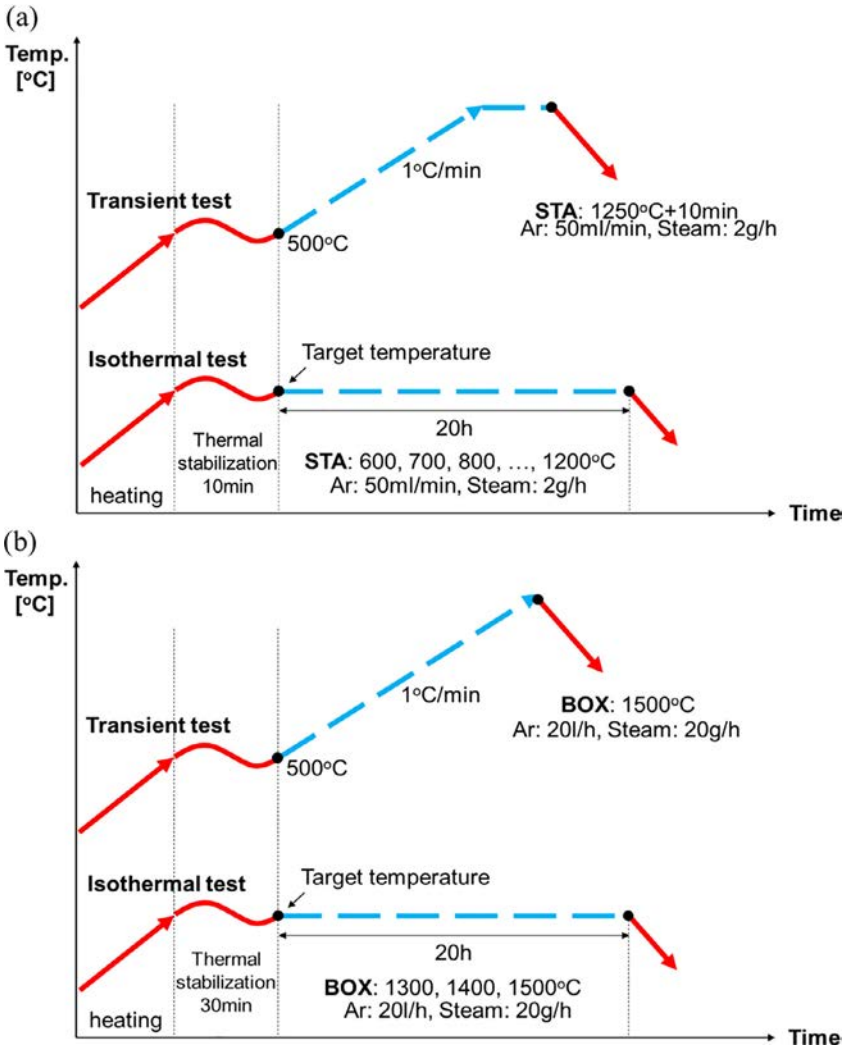

Fig. 2. The test schedules for the isothermal and transient steam oxidation in (a) STA and (b) BOX facilities.

in vol.% and H_2 release rate was converted into mol/h using Ar as a reference, since Ar release rate was constant to 20 l/h. The hydrogen release rate is proportional to the oxidation rate as following Eq (1). Eq. (2) can be derived from Eq. (1). Here, $\Delta m_{oxide}$is weight gain by oxide (M_xO_y) from the oxidation, Δm_{H_2} weight of H_2 generated by the oxidation, W_{O_2} molecular weight of O_2, W_{H_2} molecular weight of H_2. By using Eq. (2), weight gains as a function of oxidation time of nuclear-grade FeCrAl alloys were calculated.

$$xM + yH_2O \rightarrow M_xO_y + yH_2 \quad (1)$$

$$\Delta m_{oxide} : \Delta m_{H_2} = \frac{1}{2} W_{O_2} : W_{H_2} \approx 8 : 1 \quad (2)$$

The weight of specimens was measured before and after oxidation tests using an analytical balance with a resolution of 0.1 mg. To characterize microstructural features of the matrix and oxide layers, analytical methods were applied such as optical microscope (OM, Feichert Jung MeF3) and field-emission scanning electron microscopy (SEM, Philips XL30S) equipped with EDS. The phase characterization was conducted using an X-ray diffraction (XRD, Seifert PAD II) in 2θ scan mode for all oxide layers except oxides formed at 1400 °C. For oxides formed at 1400 °C, the samples were completely oxidized. Therefore, the samples were crushed into powder with which XRD analyses were performed.

3. Results

3.1. Transient oxidation tests in steam

3.1.1. Weight gains

Weight gains measured by the STA facility during the transient tests from 500 °C to 1250 °C for the four FeCrAl alloys are shown in Fig. 3a. The weight gains of two nuclear-grade alloys significantly increased between 600 and 700 °C. Then, the weight gains of the nuclear-grade alloys kept almost constant up to 800 °C for B136Y3 and 900 °C for C26M2. After the plateau region, the weight gains for B136Y3 and C26M2 increased up to 1150 °C and the slope became steeper beyond 1150 °C. For the commercial FeCrAl alloys, weight gains were almost zero up to 800 °C and rapidly increased up to 1000 °C. Then, they also exhibited a near plateau region and the weight gain slope increased again at higher temperature. Both grade alloys showed the plateau region at around 1100 °C but the region is broader for the commercial alloys than the nuclear-grade alloys. In addition, compared to the commercial FeCrAl alloys, the nuclear-grade alloys exhibited excessive weight gain at the low temperature of 600 °C.

The H_2 production of the nuclear-grade FeCrAl alloys during the transient oxidation from 500 °C to 1500 °C in the BOX facility are shown in Fig. 3b. Also, the calculated weight gain curves from H_2 production are shown in Fig. 3c, where measured weight gains af-

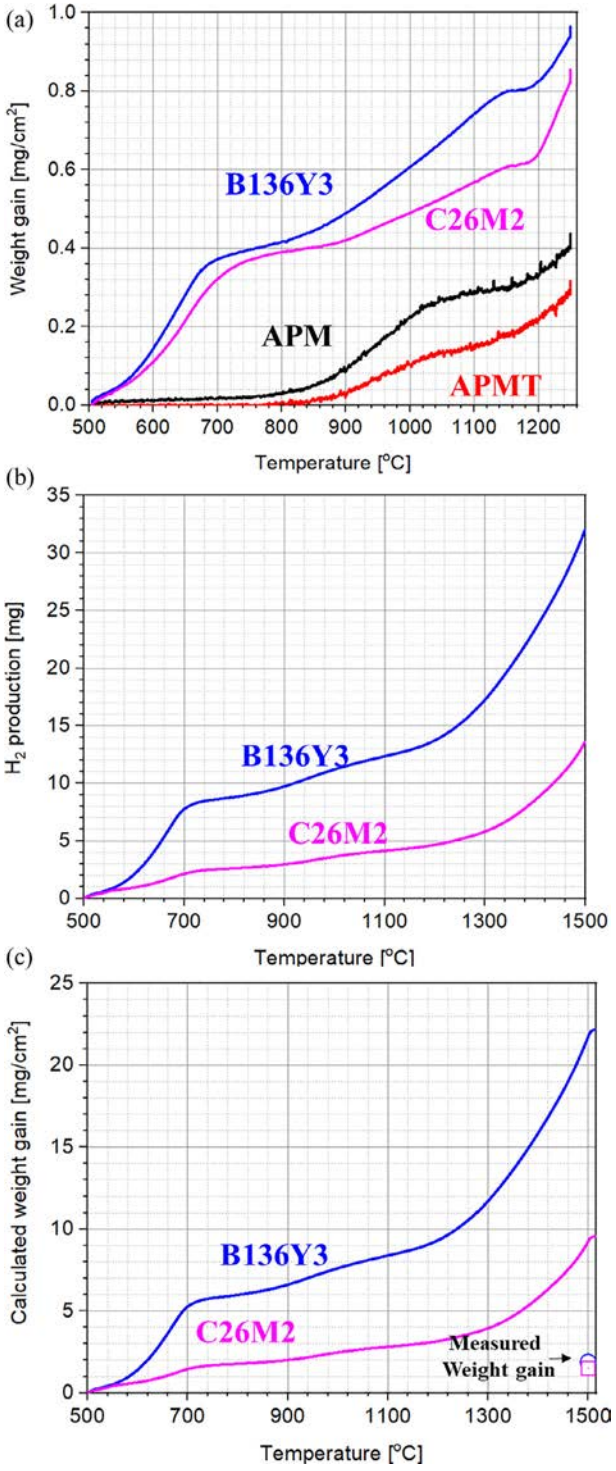

Fig. 3. Oxidation results of FeCrAl alloys during the transient steam oxidation tests: (a) weight gains from 500 °C to 1250 °C using STA facility, (b) H_2 production from 500 °C to 1500 °C using BOX facility, and (c) calculated weight gain curves from H_2 production (measured weight gains after tests are also marked.).

ter tests are marked. The weight gains up to 1250 °C (10 mg/cm^2 and 3.6 mg/cm^2 for B136Y3 and C26M2, respectively), calculated from the H_2 production, were 5∼10 times higher than the weight gains measured in the STA facility. The results in the BOX facility should be considered as semi-quantitative values due to the contribution of H_2 from other parts of the BOX facility. Nevertheless, the weight gain behaviors up to 1500 °C in BOX facility are similar to the transient oxidation behavior up to 1250 °C in STA facility. Both nuclear-grade FeCrAl alloys show significant increases in the slope at the temperatures at around 600 °C and 1200 °C like the transient oxidation test up to 1250 °C. Meanwhile, the measured weight gains after the transient oxidation test up to 1500 °C (∼2 mg/cm^2 and ∼1.5 mg/cm^2 for B136Y3 and C26M2, respectively) could be used in the estimation of oxidation kinetics later.

3.1.2. Oxide analyses

Cross-sectional SE images and EDS line scanning results for B136Y3 and C26M2 after the transient oxidation tests up to 1250 °C are shown in Figs. 4 and 5. The oxide layers for both alloys look similar to each other. The outer surface for both nuclear-grade FeCrAl alloys exhibited a single protective and continuous alumina layer. On the other hand, the oxide layer on the inner surface was different by showing bilayer structure with the outermost Fe,Al,Cr-rich oxide layer and underlying alumina layer. XRD results shown in Fig. 6 reveal that such Fe,Al,Cr-rich oxide is mixture of Fe-oxides (Fe_2O_3 and Fe_3O_4) and spinel type oxides ($FeCr_2O_4$ and $FeAl_2O_4$), while Al_2O_3 was α-phase.

Fig. 7 shows the cross-sectional optical micrographs of both nuclear-grade FeCrAl alloys after the transient oxidation test up to 1500 °C. Though the final temperature almost reached melting points [17], continuous oxide layers were formed on both alloys. The oxide layers consisted of an alumina layer on the outer surface of the tube, while the outermost Fe,Al,Cr-rich oxides and an alumina layer on the inner surface, which is similar to oxides formed in the transient oxidation test up to 1250 °C (Figs. 4 and 5). As the test temperature increased from 1250 °C to 1500 °C, the thickness of alumina on the outer surface increased from ∼3 μm (Figs. 4 and 5) to ∼8 μm (Fig. 7). However, the thickness of Fe,Al,Cr-rich oxide on the inner surface did not change significantly for C26M2. It implied that the Fe,Al,Cr-rich oxides were not formed at higher temperature from 1250 °C to 1500 °C. In addition, B136Y3 exhibited much thicker Fe,Al,Cr-rich oxide layer than C26M2, which resulted in higher weight gain of B136Y3 than C26M2 as shown in Fig. 3c.

3.2. Isothermal oxidation tests in steam

3.2.1. Weight gains and parabolic oxidation rate constants

Weight gains of two nuclear-grade FeCrAl alloys during isothermal oxidation tests at 600 °C to 1200 °C are shown in Fig. 8. Generally, as the test temperatures increased, the weight gains also increased, except at 600 °C. While the weight gain at 600 °C for B136Y3 is placed between the results obtained at 900 °C and 1000 °C, the weight gain at 600 °C for C26M2 is placed between the weight gains at 1100 °C and 1200 °C. Such high weight gain results at 600 °C are consistent with large increase in weight gain around 600 °C during the transient oxidation tests for nuclear-grade alloys as shown in Fig. 3.

Fig. 9 shows the H_2 release and calculated weight gain curves for two nuclear-grade FeCrAl alloys during the isothermal oxidation test at 1300 °C to 1500 °C. The weight gain curves were calculated based on the H_2 release rates, though semi-quantitatively. At 1300 °C, B136Y3 showed significantly higher weight gain than C26M2. Above 1400 °C, both alloys exhibited excessive oxidation behaviors as soon as steam was introduced, which can be viewed as catastrophic oxidation. After the catastrophic oxidation, the weight gains were saturated at a certain value due to the total consumption of the specimen.

Using the isothermal oxidation results, the oxidation parabolic rate constants at each temperature were derived and results are shown in Fig. 10, where alumina and Fe-oxide formation kinetics from literature [18,19] are also plotted. Both nuclear-grade alloys showed higher oxidation kinetics at 600 °C than alumina kinetics. At 700 and 800 °C, the kinetics well followed θ-alumina kinetics.

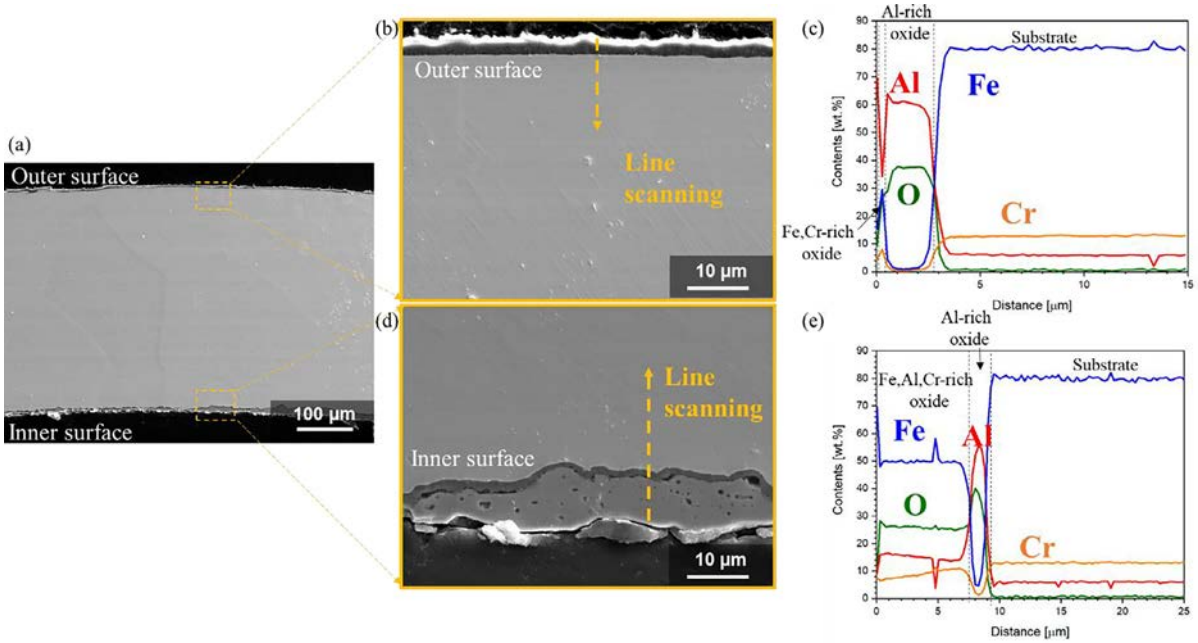

Fig. 4. Cross-sectional SEM analyses for B136Y3 after the transient steam oxidation test from 500 °C to 1250 °C: (a) Low-magnification image and high-magnification images with EDS line scanning results for (b, c) the outer surface and (d, e) the inner surface.

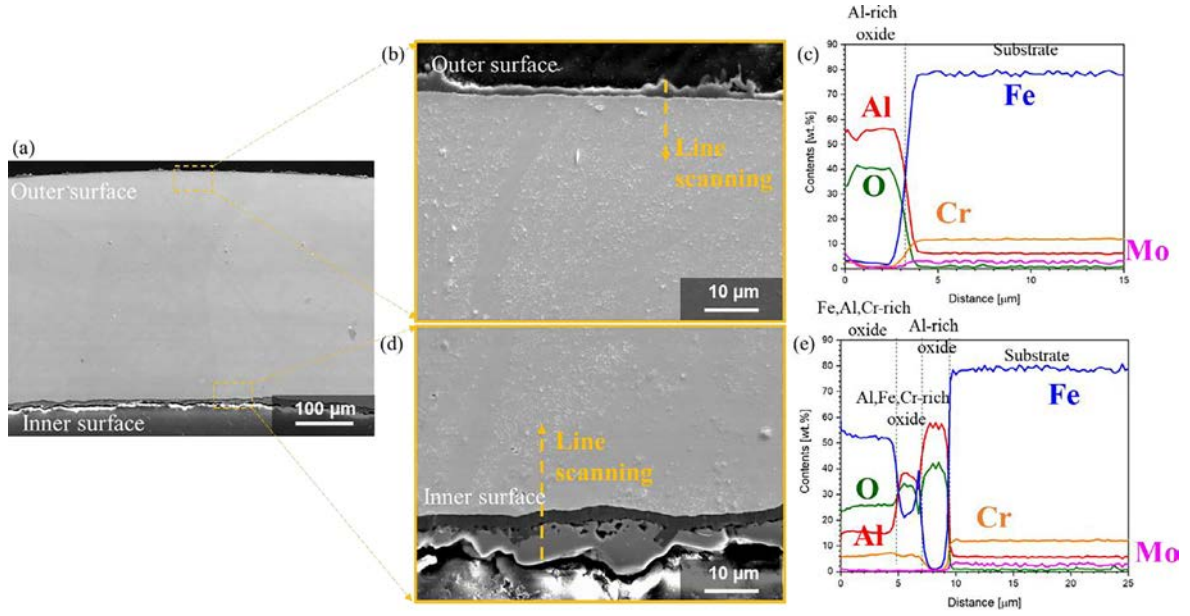

Fig. 5. Cross-sectional SEM analyses for C26M2 after the transient steam oxidation test from 500 °C to 1250 °C: (a) Low-magnification image and high-magnification images with EDS line scanning results for (b, c) the outer surface and (d, e) the inner surface.

The kinetics at 900 °C is placed between that of θ- and α-alumina. After the transient kinetics, both alloys showed α-alumina kinetics from 1000 °C to 1200 °C for B136Y3 and to 1300 °C for C26M2. As oxidation temperature further increased, the oxidation kinetics of nuclear-grade FeCrAl alloys rather matched to that of Fe-oxide, showing catastrophic oxidation.

3.2.2. Oxide analyses

Fig. 11 shows macroscopic images for two nuclear-grade FeCrAl alloys before and after isothermal steam oxidation tests at 600 °C to 1500 °C. gray oxides were formed on the tube surfaces at all oxidation temperatures. Only the inner surface of C26M2 at 600 °C was covered with some brown oxides. The tubular shapes started to be destroyed at 1400 °C, where the oxidation kinetics was beyond the α-alumina kinetics and showed catastrophic oxidation behavior.

To characterize oxides on two nuclear-grade FeCrAl alloys, cross-sectional SEM/EDS analysis was conducted. The results at 600 °C for B136Y3 are shown in Fig. 12. Different oxides were found on the outer and inner surfaces. While a very thin Al,Cr-rich oxide layer (~500 nm) was observed on the outer surface, a Cr-rich oxide layer (~4 μm) and nodular oxides were found on the inner surface. Such nodular oxides on the inner surface consisted of the outermost Fe-rich oxide and underlying Fe,Cr,Al-rich oxides. Cross-sectional SEM/EDS analysis results of C26M2 after isothermal oxidation at 600 °C are shown in Fig. 13. Similar with B136Y3, a very thin Al,Cr-rich oxide layer on the outer surface and thick Fe-rich oxide layers on the inner surface were observed. Here, the Fe-rich

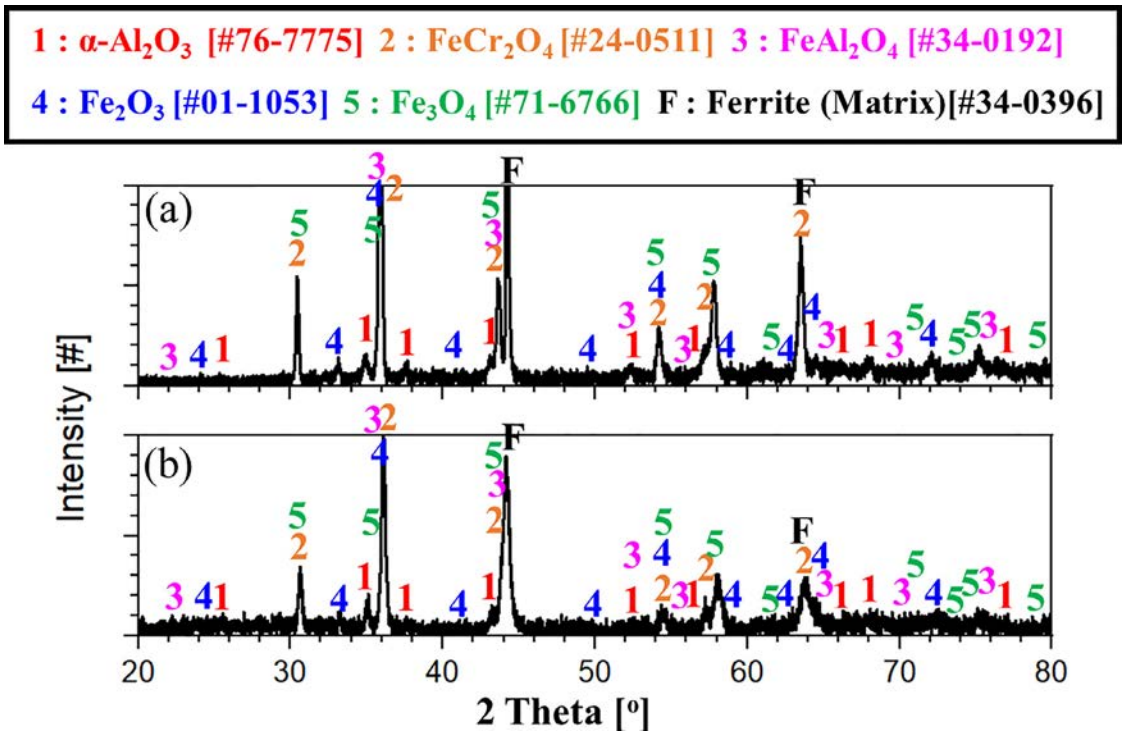

Fig. 6. XRD results of the inner surfaces for (a) B136Y3 and (b) C26M2 after the transient steam oxidation test from 500 °C to 1250 °C.

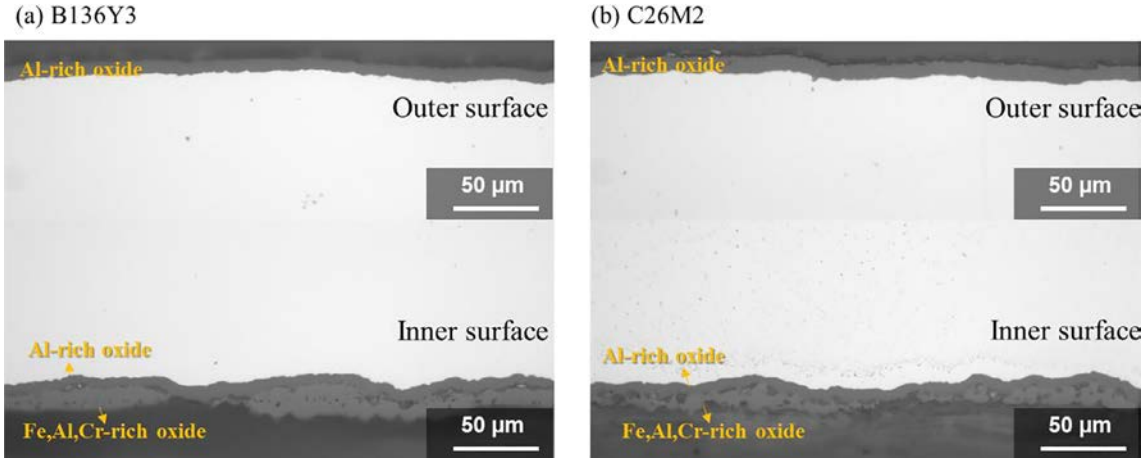

Fig. 7. Cross-sectional optical micrographs for (a) B136Y3 and (b) C26M2 after the transient steam oxidation test from 500 °C to 1500 °C.

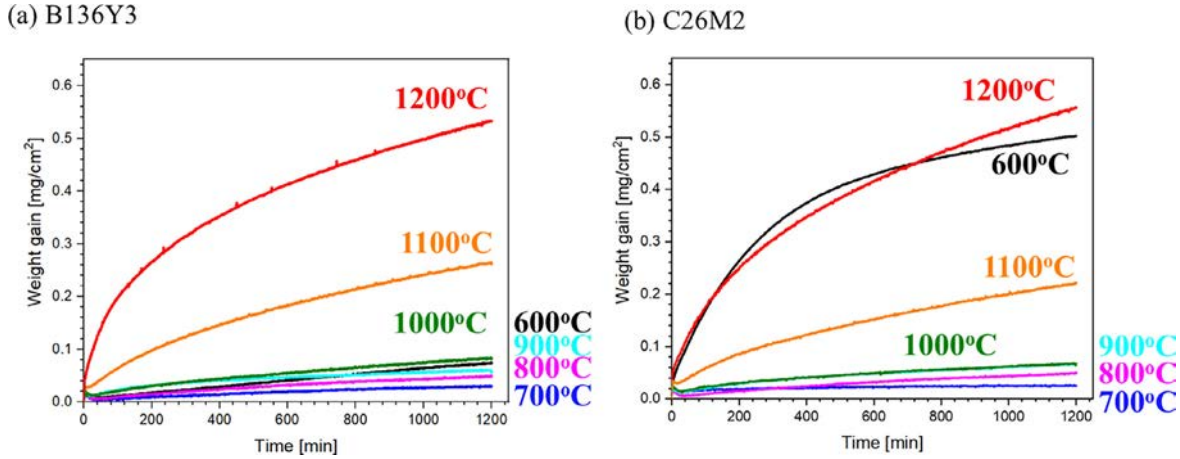

Fig. 8. Weight gains of (a) B136Y3 and (b) C26M2 during the isothermal steam oxidation tests at 600 °C to 1200 °C for 20 h.

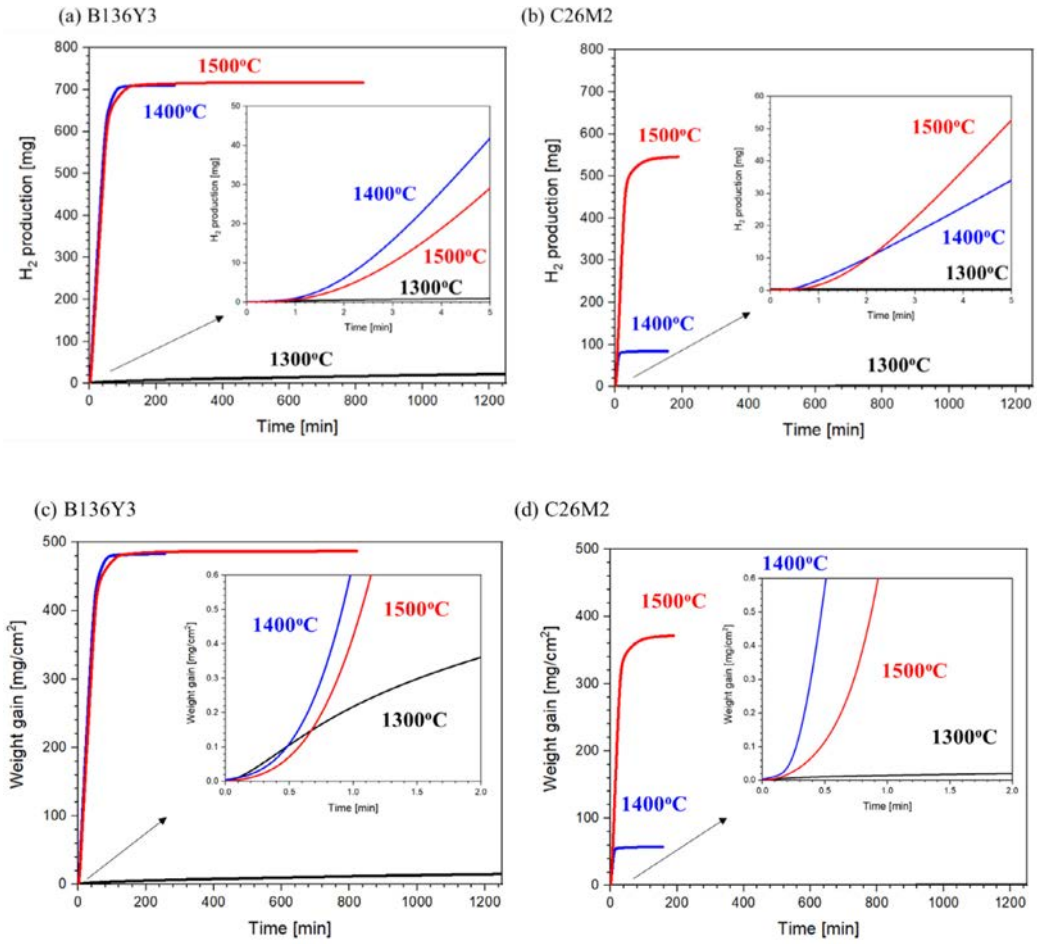

Fig. 9. H_2 production and calculated weight gain curves during the isothermal steam oxidation tests at 1300 °C to 1500 °C using the BOX facility: (a, c) B136Y3 and (b, d) C26M2, respectively.

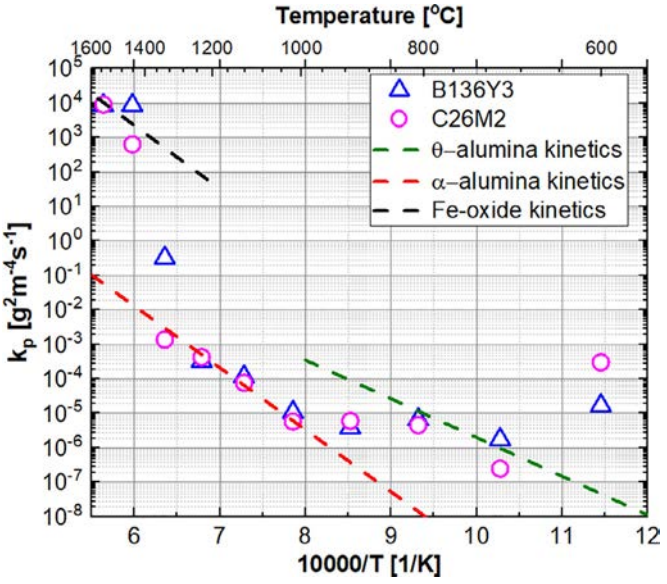

Fig. 10. Parabolic rate constants of B136Y3 and C26M2 as a function of temperature with the parabolic constants of Fe-oxide [18], α-alumina [18] and θ-alumina [19].

oxide layer consisted of a Fe-oxide layer (~7 μm) and underlying a Fe,Cr,Al-rich oxide layer (~7 μm).

Figs. 14 and 15 show XRD results of B136Y3 and C26M2, respectively, after isothermal oxidation tests at each temperature for 20 h. The inner surface was analyzed only for C26M2 after isothermal oxidation at 600 °C, while outer surfaces were analyzed for the others. As shown in the XRD results, the peaks from the outer surface of the two alloys after isothermal oxidation at 600 °C mainly matched to the matrix due to a very thin outer oxide layer. However, the inner surface of C26M2 (Fig. 15a) exhibited peaks of Fe_2O_3, $Fe(Fe,Cr,Al)_2O_4$ and Al_2O_3, since the Fe-oxide layer and Fe,Cr,Al-rich oxide layer were relatively thick (~14 μm) as shown in Fig. 7b. As considering the XRD result, Fe-oxide is most probably Fe_2O_3 and Fe_3O_4 and the underlying Fe,Cr,Al-rich oxide is spinel type oxide. Though the two nuclear-grade FeCrAl alloys showed a very thin Al,Cr-rich oxide layer on the outer surfaces, oxide layers on the inner surfaces were different. That is, B136Y3 showed the Cr-rich oxide layer with the Fe-rich nodular oxides, C26M2 exhibited a continuous and thick Fe-oxide, and underlying Fe,Cr,Al-rich oxide layers. Such continuous and thick Fe-oxide and underlying Fe,Cr,Al-rich oxides on the inner surface of C26M2 resulted in the large weight gain at 600 °C in Fig. 8.

As the oxidation temperature increased to 700 °C, Fe-rich oxides were not found on the inner surface for the both alloys (Fig. 16). The oxide layers on both inner and outer surfaces were too thin to be detected by OM. Such results well agree with the XRD results in Figs. 14b and 15c, where oxide peaks were hardly observed due to the thin oxide layers. In addition, weight gain results for the two nuclear-grade FeCrAl alloys (Fig. 8) showed the lowest weight gain at 700 °C among isothermal oxidation tests. As the oxidation temperature increased from 900 °C to 1300 °C, small peaks for α-alumina were found and the intensity increased.

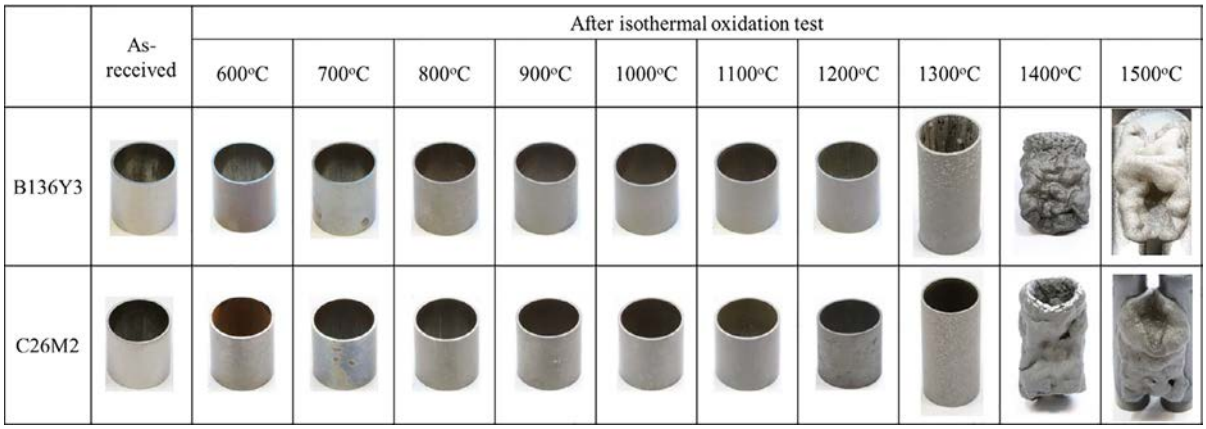

Fig. 11. Macroscopic images for two nuclear-grade FeCrAl alloys before and after the isothermal steam oxidation at 600 °C to 1500 °C for 20 h.

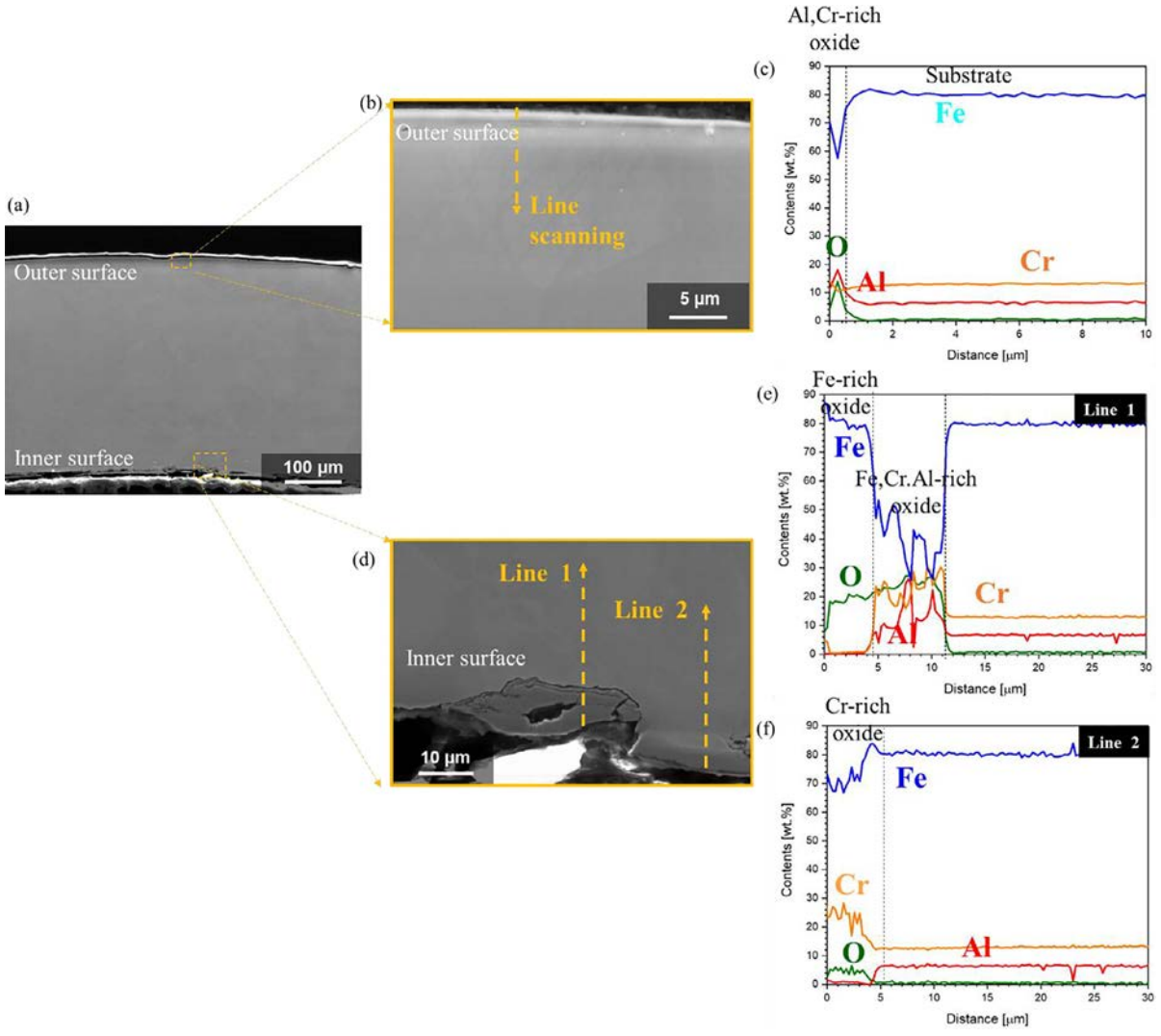

Fig. 12. Cross-sectional SEM analyses for B136Y3 after the isothermal steam oxidation at 600 °C for 20 h: (a) Low-magnification image and high-magnification images with EDS line scanning results for (b, c) the outer surface and (d, e, f) the inner surface.

Although the oxidation kinetics (Fig. 10) and the macroscopic images (Fig. 11) are different at 1300 °C for two alloys, the XRD peaks for the alloys were similar by showing strong α-alumina peaks. To confirm the XRD results, cross-sectional SEM/EDS analysis was conducted for B136Y3 after the isothermal oxidation test at 1300 °C and the results are shown in Fig. 17. Convoluted alumina layers were formed on inner and outer surfaces of B136Y3. Since the convoluted alumina is more prone to localized carking and become less protective, thickness of the alumina layer depends on the location. Multi-layered alumina was formed on some location as shown in Fig. 17b. If the localized cracking did not occur, an alumina layer was formed with a thickness of around 8 μm

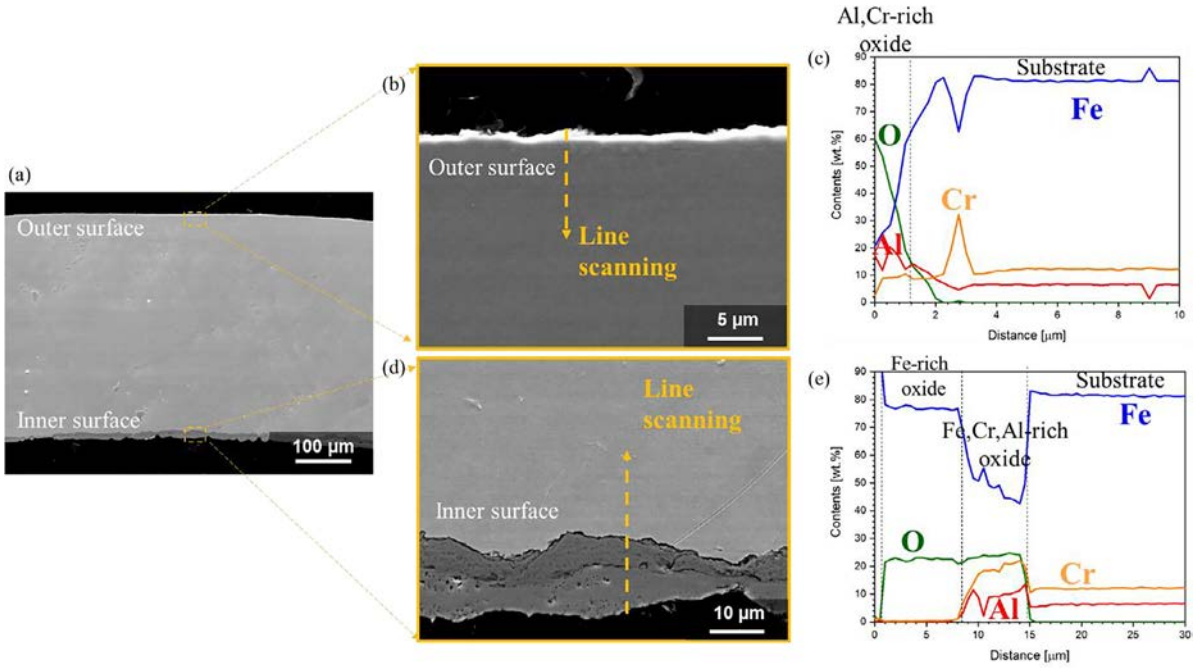

Fig. 13. Cross-sectional SEM analyses for C26M2 after the isothermal steam oxidation at 600 °C for 20 h: (a) Low-magnification image and high-magnification images with EDS line scanning results for (b, c) the outer surface and (d, e) the inner surface.

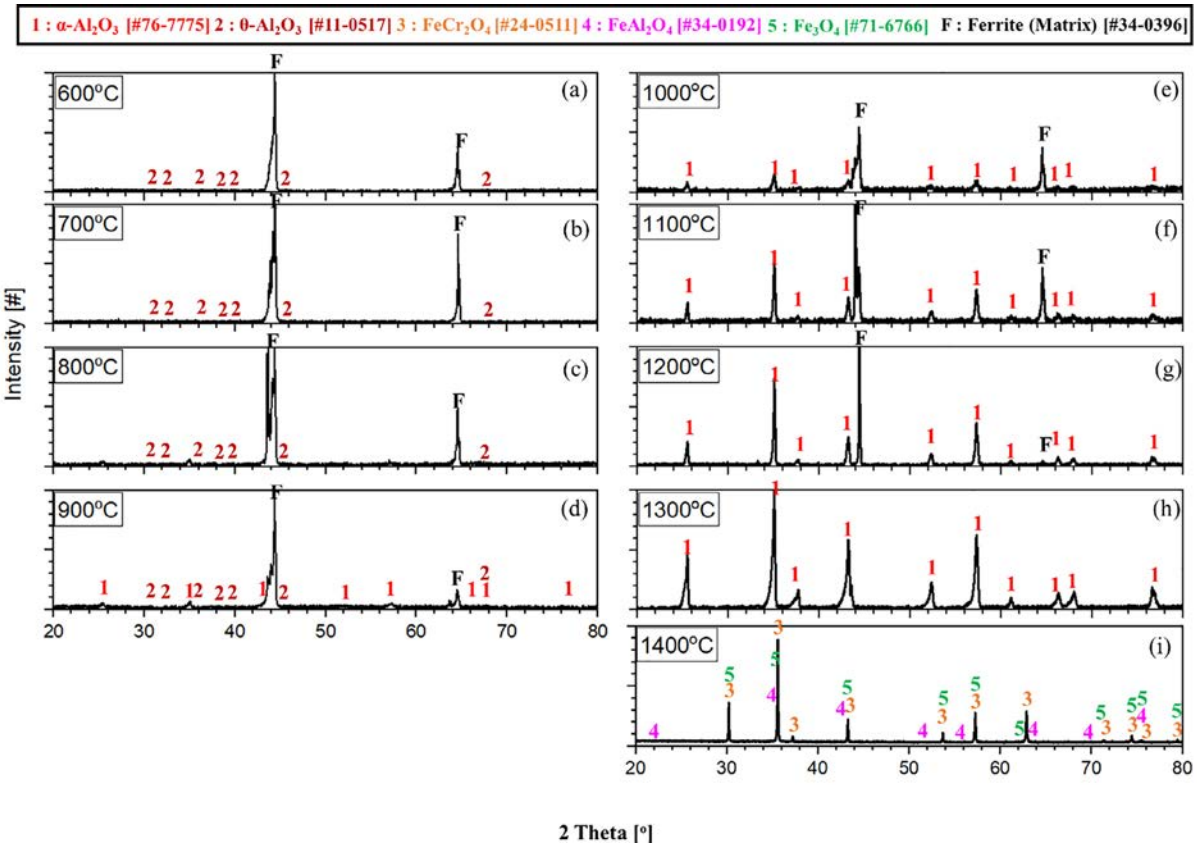

Fig. 14. XRD results of the outer surfaces for B136Y3 tube after the isothermal steam oxidation at 600 °C to 1400 °C for 20 h.

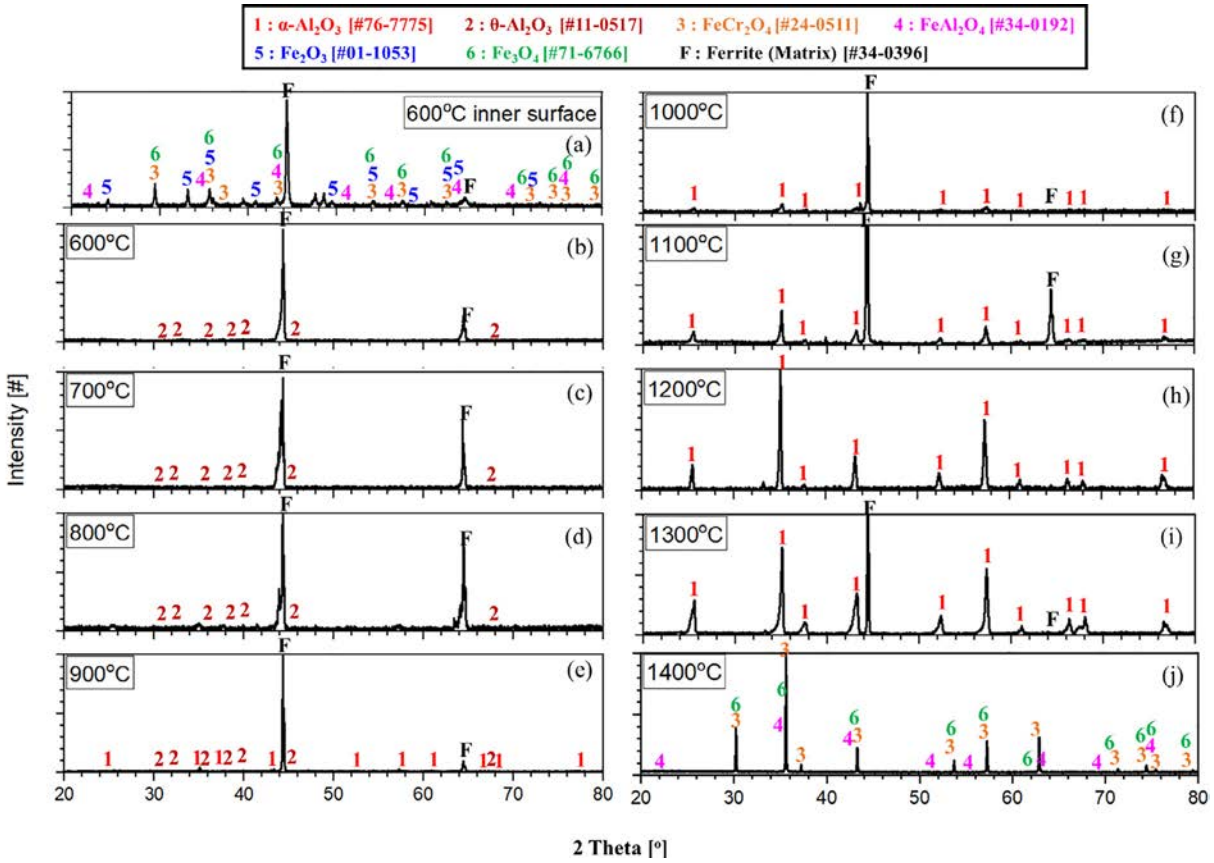

Fig. 15. XRD results of (a) the inner surface for C26M2 after isothermal steam oxidation at 600 °C for 20 h and (b-j) the outer surfaces for C26M2 after isothermal steam oxidation at 600 °C to 1400 °C for 20 h.

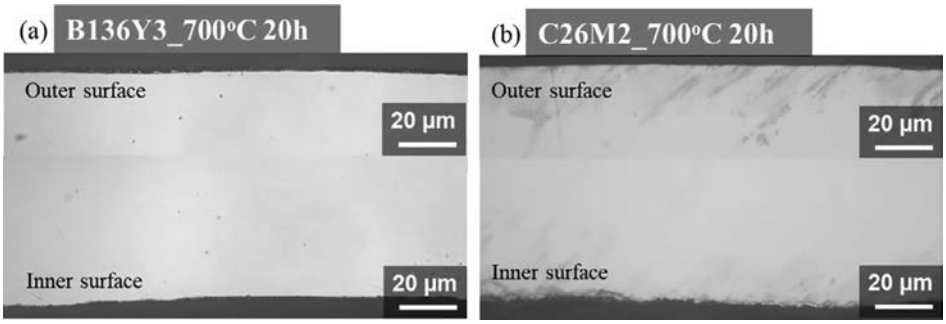

Fig. 16. Cross-sectional optical micrographs for (a) B136Y3 and (b) C26M2 tubes after the isothermal steam oxidation at 700 °C for 20 h.

(Fig. 17d). On the other hand, C26M2 shows continuous and well-attached alumina layers on inner and outer surfaces with a thickness of approximately 8 μm (Fig. 18). Through the oxide analyses, it is revealed that the convoluted alumina and oxide spallation during the steam oxidation resulted in faster kinetics of B136Y3 than C26M2 at 1300 °C.

As shown in the macroscopic images (Fig. 11), the samples were totally oxidized above 1400 °C by showing the catastrophic oxidation behavior. After the catastrophic oxidation, XRD results show sharp peaks of spinel oxides (Figs. 14i and 15j). To analyze oxides formed above 1400 °C and investigate the early stage of the catastrophic oxidation, C26M2 was exposed at 1500 °C in the BOX facility, then the furnace was shut down as soon as the excessive H_2 generation was detected (the oxidation time was approximately 280 s). Fig. 19 shows the macroscopic image, cross-sectional back-scattered SE (BSE) images and EDS line scanning results of a C26M2 tube after steam oxidation test at 1500 °C for 280 s. As shown in the macroscopic image, the excessive oxidation was predominantly started at the edge and some localized points beyond the edge area. To investigate both non-excessive and excessive oxidation behaviors, the SEM-EDS analysis was conducted for two regions, the middle and the edge of the tube specimen. For the middle of the specimen, oxide layers consisted of the outermost Fe,Al oxides and an underlying alumina. On the other hand, the oxides formed at the edge were significantly different from those formed in the middle region as shown in Fig. 19c. Thick Fe,Cr,Al oxides were formed at the outermost and complex Al,Cr-rich oxides with Fe with small amount of Mo were present underneath the Fe,Cr,Al-rich oxides. Alumina was internally formed at the oxide/metal interface. Depletion of Cr and Al was found by EDS line scanning at the oxide/metal interface (Fig. 19e). The Cr and Al contents were recovered to original Al and Cr contents, 6 wt.% and 12 wt.% respectively, at the middle of tube specimen.

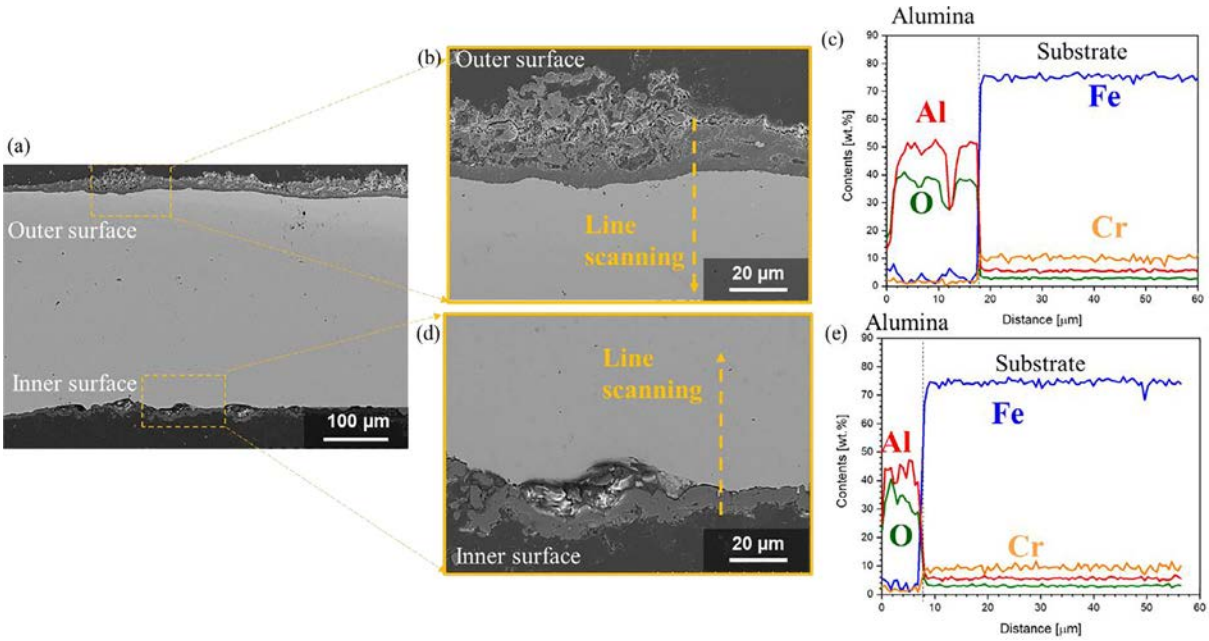

Fig. 17. Cross-sectional SEM analyses for B136Y3 after the isothermal steam oxidation at 1300 °C for 20 h: (a) Low-magnification image and high-magnification images with EDS line scanning results for (b, c) the outer surface and (d, e) the inner surface.

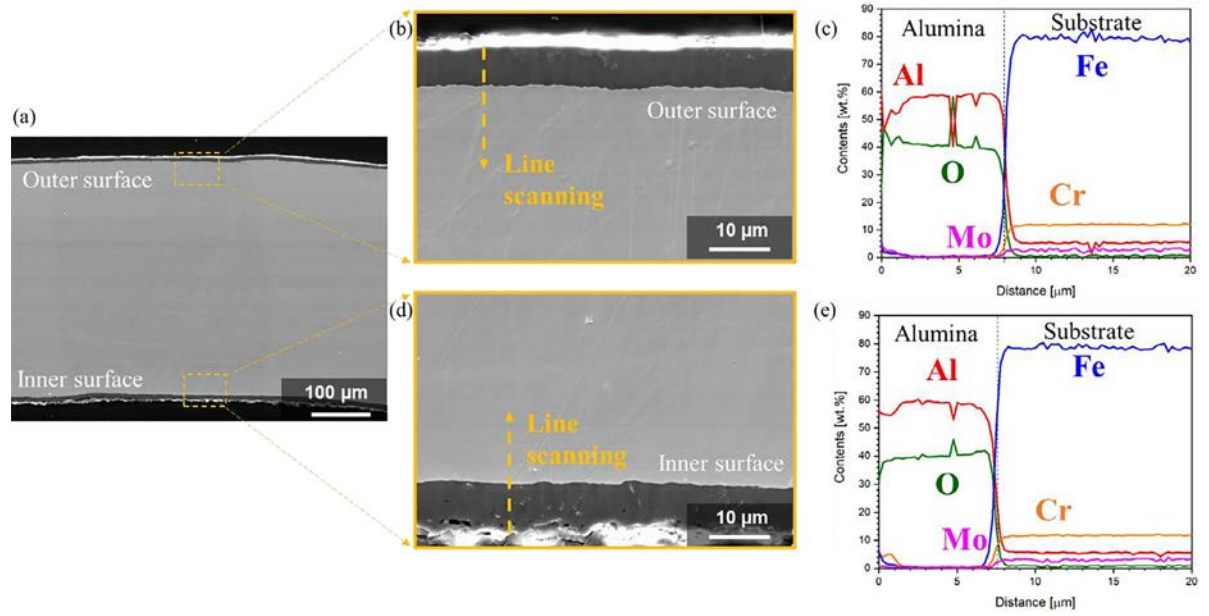

Fig. 18. Cross-sectional SEM analyses for C26M2 after the isothermal steam oxidation at 1300 °C for 20 h: (a) Low-magnification image and high-magnification images with EDS line scanning results for (b, c) the outer surface and (d, e) the inner surface.

The Mo content in the matrix was maintained at approximately 2 wt.% while Mo was hardly observed in oxide layers. In addition, Mo-rich flakes were found at the outlet of the test zone (not shown in the paper) for samples showing catastrophic oxidation. Such observation implied the volatilization of Mo-oxides, which are volatile above 800 °C in steam [20]. Al is selectively oxidized at high temperature and protective alumina also prevented the Mo oxidation. Thus, the volatilization of Mo-oxides was not significant before the alumina layer was failed. However, the catastrophic oxidation caused entire oxidation of the alloy including Mo. Therefore, Mo oxides were evaporated and condensed at the colder outlet of the test zone.

4. Discussion

4.1. Different oxides on inner and outer surfaces at 600 °C

As shown in the transient oxidation results (Figs. 4, 5, and 7) and isothermal oxidation results at 600 °C (Figs. 12 and 13), the oxidation behaviors on the inner and outer surfaces of the tube specimens were different. Surface treatment could be one of the factor affecting such different oxidation behaviors. Fig. 20 shows the BSE images and EDS line scanning results of the as-received C26M2 tube. In the low magnification images (Figs. 20a and 20d), the inner surface shows higher roughness than the outer surface.

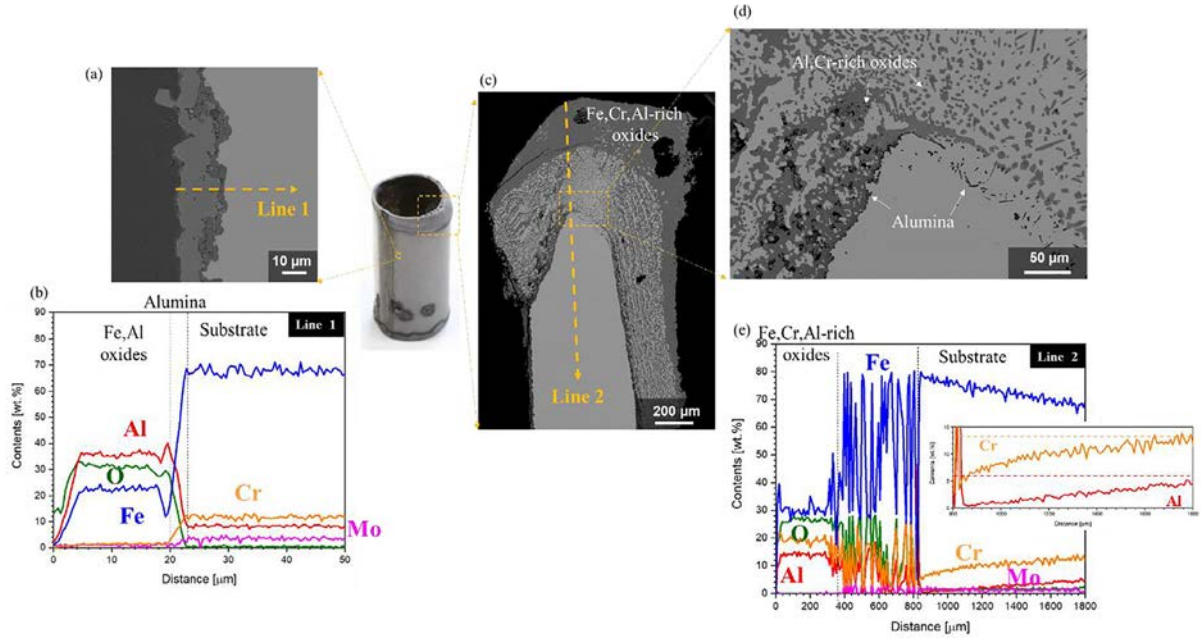

Fig. 19. Macroscopic image, cross-sectional BSE micrographs and EDS line scanning results for (a, b) the outer surface apart from the edge and (c, d, e) the edge of the C26M2 tube after the isothermal steam oxidation at 1500 °C for a short period of time.

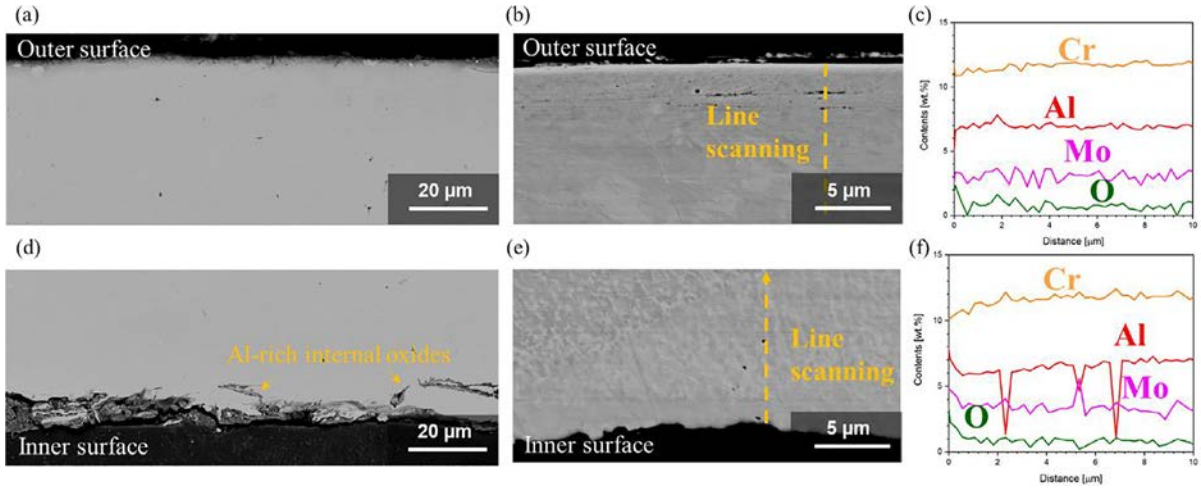

Fig. 20. Cross-sectional BSE micrographs and EDS line scanning results for (a-c) the outer surface and (d-f) the inner surface of the as-received C26M2 tube.

In addition, more internal oxides were present on the inner surface, which were enriched in Al and Cr. The formation of internal oxides would result in slightly depleted Cr near the inner surface and Al at the grain boundaries (Fig. 20f). Such Cr and Al depletion can cause the formation of Fe-rich oxides on the inner surface.

Furthermore, while B136Y3 and C26M2 alloys showed similar weight gain at low temperature for the transient oxidation test up to 1250 °C (Fig. 3a), B136Y3 exhibited higher weight gain at low temperature for the transient oxidation test up to 1500 °C (Fig. 3b) and C26M2 exhibited higher weight gain at 600 °C for the isothermal oxidation test (Fig. 8). Such non-reproducible oxidation results at the low temperature range also implied that the enhanced oxidation on the inner surfaces is not due to the chemical compositions of the two alloys. It is mostly caused by some defects from the tube production process.

Meanwhile, the different oxidation behaviors on inner and outer surfaces disappeared above 700 °C as shown in Fig. 16. As the temperature increased from 600 °C to 700 °C, the Al diffusivity increases approximately 100 times in BCC [21], but the oxidation parabolic rate constant increases 5 times for a Fe-21Cr-5Al alloy in dry air [22]. Because Al supply by diffusion is faster than Al consumption by alumina formation above 700 °C, a continuous alumina layer can be produced. Therefore, different oxidation behaviors on the inner and outer surfaces were not found by increasing the oxidation temperature above 700 °C.

Nevertheless, the enhanced oxidation behavior on the inner surface can be mitigated by grinding similar to the outer surface. In addition, for application as nuclear fuel claddings, the inner surface will not be exposed to steam at lower temperature. Only when the burst of cladding occurs, the inner surface can be exposed to steam. However, the burst temperatures are usually above 800 °C for the nuclear-grade FeCrAl alloy [23], where the different oxidation behaviors will disappear.

4.2. Steam oxidation kinetics of nuclear-grade FeCrAl alloys

As discussed in the previous section, the rapid oxidation rate at 600 °C on the inner surface of nuclear grade FeCrAl alloys was

Table 2
Oxidation kinetics data for nuclear-grade FeCrAl alloys in the temperature range of 600–1500 °C.

	Experimental data		Reference	
Temperature range	Materials	$k^{0.5}$ [g/m^2-s$^{0.5}$]	$k^{0.5*}$ [g/m^2-s$^{0.5}$]	Oxide
600 °C	B136Y3	4.1×10^{-3}	–	–
	C26M2	1.7×10^{-2}		
700 °C	B136Y3	1.3×10^{-3}	1.0×10^{-3} at 700 °C	Transient alumina [19]
	C26M2	5.0×10^{-4}		
800 °C	B136Y3	2.6×10^{-3}		
	C26M2	2.1×10^{-3}		
900 °C	B136Y3	1.9×10^{-3}	–	–
	C26M2	2.4×10^{-3}		
1000 °C	B136Y3	3.3×10^{-3}	2.5×10^{-3} at 1000 °C	α-alumina [18]
	C26M2	2.39×10^{-3}		
1100 °C	B136Y3	1.1×10^{-2}		
	C26M2	8.7×10^{-3}		
1200 °C	B136Y3	1.8×10^{-2}		
	C26M2	2.1×10^{-2}		
1300 °C	B136Y3	5.7×10^{-1}		
	C26M2	3.7×10^{-2}		
1400 °C	B136Y3	9.2×10	5.0×10 at 1400 °C	Fe-oxide [18]
	C26M2	2.5×10		
1500 °C	B136Y3	9.1×10		
	C26M2	9.5×10		

* calculated value by using equation in references.

most probably resulted from the tube manufacturing process and it can be suppressed. Therefore, without the rapid oxidation at 600 °C, the oxidation kinetics of nuclear-grade FeCrAl alloys can be divided into three temperature ranges, T < 900 °C, 1000 °C < T < 1300 °C, T > 1400 °C in Fig. 10. The kinetics and oxides are summarized in Table 2.

In the temperature range of T < 900 °C, the oxide analyses could not define the oxide phases because of too thin oxide layer. However, the oxidation kinetics well matched to the reported kinetics of the θ-alumina, a transient alumina [19]. Such transient alumina kinetics exhibits around 2 orders of magnitude faster than α-alumina. The transient and α-alumina are competitively formed at around 900 °C [12,24]. Thus, similar kinetics are shown at 800, 900 and 1000 °C in Fig. 10, even the oxidation temperature increases.

In the temperature range of 1000 °C < T < 1300 °C, α-alumina was observed as shown in Figs. 14 and 15. Also, the results obtained in this study well match to the reported α-alumina kinetics [18]. In this temperature range, both nuclear-grade FeCrAl alloys show excellent oxidation resistance as an ATF cladding by showing around 5 orders of magnitude lower oxidation kinetics compared with current Zr alloys [18]. At 1300 °C, both nuclear-grade FeCrAl alloys exhibited α-alumina formation but different kinetics. While convoluted alumina layers were formed on B136Y3, a well-attached and flat alumina layer was produced on C26M2. Quadakkers et al. [25] conducted air oxidation tests at 1000 °C and 1100 °C with wrought and oxide-dispersed Fe-20Cr-5Al alloys. Through the oxidation tests, it was found that ODS exhibited more adherent and flat alumina than the wrought alloy. It was indicated that the improved adherence of alumina on ODS resulted from the suppressed outward diffusion by yttria addition. On the other hand, Dryepndt et al. [26] observed more convoluted alumina morphology on Fe-Al with lower strength and at higher temperature. They explained that such convoluted alumina morphology results from lower strength of the matrix. Also, because strength is reduced by increasing temperature, more convoluted alumina at higher temperature can be explained by strength effect of the matrix. In addition, different alumina morphology in ref. [25] can be explained by the strength effect, since ODS have higher strength than wrought alloys. For the nuclear-grade FeCrAl alloys, because both alloys contain similar Y content in a matrix, Y addition would not be the main reason for the different alumina morphology. It is reported that C26M2 has higher strength than B136Y3 by adding Mo [6]. Therefore, it seems that B136Y3 exhibited the convoluted alumina morphology at relatively low temperature of 1300 °C than C26M2 due to its lower strength (Fig. 17). In addition, thicker alumina layers were found on the outer surfaces, because the tube outer surface is more susceptible to the tensile stress and oxide cracking during oxidation.

Above 1400 °C, the nuclear-grade FeCrAl alloys were quickly oxidized by following Fe-oxide kinetics as shown in Fig. 10. After the catastrophic oxidation, tube shapes were totally destroyed (Fig. 11) and XRD measurement confirmed the growth of Fe,Cr-rich spinel oxides (Figs. 14i and 15j). Such completely oxidized tubes would be no barrier against the release of fission products anymore, and result in more severe accident consequence by increasing the reactor core temperature. However, it has been reported that a protective alumina layer is formed on low-Cr ODS FeCrAl alloys even at 1400 °C [13,27,28]. ODS steels itself have positive effect on high-temperature oxidation resistance owing to fast Cr and/or Al supply via fine-grain boundaries [29]. Besides the fine grains, higher strength of low-Cr ODS FeCrAl can affect the high temperature oxidation behavior. As mentioned previously, convoluted alumina morphology can be more observed on alloys with lower strength and can cause oxide spallation during oxidation. Thus, the lower strength of wrought nuclear grade FeCrAl alloys results in the decrease of maximum temperature to produce a protective alumina.

4.3. Catastrophic oxidation behavior of nuclear-grade FeCrAl alloys above 1400 °C

To understand the initial catastrophic oxidation behavior and mitigate the excessive oxidation for the nuclear-grade FeCrAl tubes, C26M2 exposed to 1500 °C for a short time was investigated. Based on the oxide analyses, the catastrophic oxidation at very high temperature can be explained as follows. When nuclear-grade FeCrAl alloys are exposed to very high-temperature steam, Al,Fe-spinel oxides are produced and alumina is formed underneath the spinel

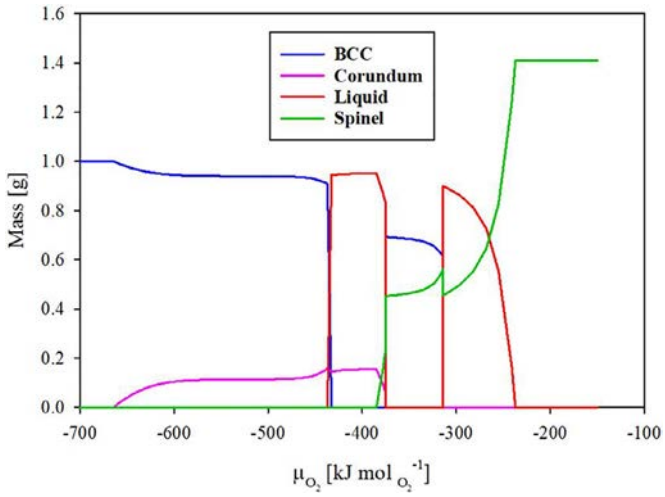

Fig. 21. Stable phase fraction in the Fe-Cr-Al-O system for Fe-12Cr-6Al at 1400 °C as a function of oxygen chemical potential [28].

oxides. When the underlying alumina is connected and become continuous, the spinel oxide formation is suppressed. In this stage, Cr and Al contents are not depleted yet as shown in Fig. 19b. However, the underlying alumina is convoluted at very high temperature and easy to be spalled off. When oxides are spalled off and the spallation is repeated, Cr and Al would be depleted in the substrate. As a results, Fe,Cr,Al-rich spinel oxides are produced. Such spinel oxides would become much thicker than the initial spinel oxides, because there is no underlying alumina to suppress the formation of spinel oxides. Therefore, thick Fe,Cr,Al-rich oxides were formed as shown in Figs. 19c-e.

The oxides at the edge can be divided into four regions; Fe,Cr,Al-rich oxides with pores, Al,Cr-rich oxides and Fe,Mo-rich phase with pores, alumina, substrate. These regions exactly match to phase diagrams of the Fe-Cr-Al-O system depending on oxygen partial pressure that was calculated at 1500 °C with TAF-ID [17] and at 1400 °C with CALPHAD [28]. The phase diagram (Fig. 21) show that the stable phases at the very high temperature are varying with oxygen partial pressure, such that spinel oxides, liquid and spinel oxides, BCC and spinel oxides, liquid and corundum, BCC and corundum, and BCC as the oxygen partial pressure decreases. Here, the liquid phase is most probably FeO, which melts at 1377 °C and it would make pores by cooling in the spinel and corundum regions. Such pores can also be found in the spinel and near α-alumina (corundum) phases. In addition, it seems that the liquid phase is the most destroying factor of tube shapes.

Nevertheless, it is a promising result that the transient oxidation result did not show the catastrophic oxidation even at 1500 °C and the catastrophic oxidation was started mostly from the edge of the tube. In severe accidents, claddings will be oxidized from the operating temperature to very high temperature like in the transient oxidation tests. In addition, both ends of cladding tubes are enclosed with end-caps and FeCrAl alloys showed higher burst and ballooning resistance than Zr-alloys [23,30]. Therefore, the catastrophic oxidation will be delayed in the nuclear accidents despite catastrophic oxidation was observed in the isothermal oxidation tests at 1400 °C and 1500 °C.

5. Conclusions

The oxidation mechanisms and kinetics in steam of two nuclear-grade FeCrAl alloys (B136Y3 and C26M2) were investigated with transient tests from 500 °C up to 1500 °C of 1 °C/min and isothermal tests from 600 °C to 1500 °C for 20 h. Based on the oxidation tests and subsequent analyses, the following conclusions are drawn:

- While transient oxidation tests up to 1500 °C did not show geometrical change of the nuclear-grade FeCrAl tubes, the isothermal oxidation tests above 1400 °C show the completely-oxidized and totally-destroyed tubes.
- At 600 °C, oxidation kinetics was faster than some higher temperatures, which is caused by the formation of Fe-rich oxides on the inner tube surface. On the other hand, Al-rich oxide layer was observed on the outer surface. The different oxidation behaviors on inner and outer surface most probably result from different surface conditions.
- At 700 °C to 900 °C, an Al-rich oxide layer was formed on both surfaces. The oxidation kinetics of nuclear-grade FeCrAl well followed that of transient alumina. From 1000 °C to 1300 °C, a continuous and protective alumina layer was found on the nuclear-grade FeCrAl alloys showing α-alumina kinetics.
- Above 1400 °C, the nuclear-grade FeCrAl tube specimens were quickly and completely oxidized (i.e. catastrophic oxidation) by exhibiting Fe-oxide kinetics as soon as steam was introduced. Failure of the protective alumina layer causes depletion of Cr and Al and excessive formation of Fe-rich spinel oxide. During catastrophic oxidation, FeO liquid phase formation seems to cause significant geometrical change of tube specimens.

Data availability

The raw/processed data required to reproduce these findings cannot be shared at this time. They will be shared upon request to the corresponding author.

Declaration of Competing Interest

The authors declare that they have no known competing financial interests or personal relationships that could have appeared to influence the work reported in this paper.

CRediT authorship contribution statement

Chaewon Kim: Formal analysis, Investigation, Writing – original draft. **Chongchong Tang:** Investigation, Writing – review & editing. **Mirco Grosse:** Formal analysis. **Yunhwan Maeng:** Formal analysis. **Changheui Jang:** Supervision, Writing – review & editing. **Martin Steinbrueck:** Conceptualization, Writing – review & editing.

Acknowledgments

This study was supported by the HGF nuclear safety program NUSAFE at KIT of Germany, the Nuclear Global Internship Program though the Korea Nuclear International Cooperation Foundation (KONICOF) funded by the Ministry of Science and ICT, and MOTIE/KETEP project (No. 20171510101990) of the republic of Korea. The authors appreciate the Oakridge National Laboratory (ORNL) for the supply of the nuclear-grade FeCrAl alloy cladding tubes. We thank U. Stegmaier, P. Severloh and B. Choi for their technical support during experiments.

References

[1] K.A. Terrani, Accident tolerant fuel cladding development: promise, status, and challenges, J. Nucl. Mater. 501 (2018) 13–30, doi:10.1016/j.jnucmat.2017.12.043.
[2] C. Tang, M. Stueber, H.J. Seifert, M. Steinbrueck, Protective coatings on zirconium-based alloys as accident-tolerant fuel (ATF) claddings, Corros. Rev. 35 (3) (2017) 141–165, doi:10.1515/corrrev-2017-0010.
[3] Z. Duan, H. Yang, Y. Satoh, K. Murakami, S. Kano, Z. Zhao, J. Shen, H. Abe, Current status of materials development of nuclear fuel cladding tubes for light water reactors, Nucl. Eng. Des. 316 (2017) 131–150, doi:10.1016/j.nucengdes.2017.02.031.

[4] J.-.C. Brachet, E. Rouesne, J. Ribis, T. Guilbert, S. Urvoy, G. Nony, C.T.- Masclet, M.L. Saux, N. Chaabane, H. Palancher, A. David, J. Bischoff, J. Augereau, E. Pouilier, High temperature steam oxidation of chromium-coated zirconium-based alloys: kinetics and process, Corros. Sci. 167 (2020) 108537, doi:10.1016/j.corsci.2020.108537.

[5] H. Kim, H. Jang, G.O. Subramanian, C. Kim, C. Jang, Development of alumina-forming duplex stainless steels as accident-tolerant fuel cladding materials for light water reactors, J. Nucl. Mater. 507 (2018) 1–14, doi:10.1016/j.jnucmat.2018.04.027.

[6] Y. Yamamoto, B.A. Pint, K.A. Terrani, K.G. Field, Y. Yang, L.L. Snead, Development and property evaluation of nuclear grade wrought FeCrAl fuel cladding for light water reactors, J. Nucl. Mater. 467 (2) (2015) 703–716, doi:10.1016/j.jnucmat.2015.10.019.

[7] B.A. Pint, K.A. Terrani, M.P. Brady, T. Cheng, J.R. Keiser, High temperature oxidation of fuel cladding candidate materials in steam-hydrogen environments, J. Nucl. Mater. 440 (1–3) (2013) 420–427, doi:10.1016/j.jnucmat.2013.05.047.

[8] K.A. Unocic, Y. Yamamoto, B.A. Pint, Effect of Al and Cr content on air and steam oxidation of FeCrAl alloys and commercial APMT alloy, Oxid. Met. 87 (2017) 431–441, doi:10.1007/s11085-017-9745-1.

[9] C. Tang, A. Jianu, M. Steinbrueck, M. Grosse, A. Weisenburger, H.J. Seifert, Influence of composition and heating schedules on compatibility of FeCrAl alloys with high-temperature steam, J. Nucl. Mater. 511 (2018) 496–507, doi:10.1016/j.jnucmat.2018.09.026.

[10] N. Li, S.S. Parker, T.A. Saleh, S.A. Maloy, A.T. Nelson, Intermediate temperature corrosion behavior of Fe-12Cr-6Al-2Mo-0.2Si-0.03Y alloy (C26M) at 300-600 °C, Corros. Sci. 157 (2019) 274–283, doi:10.1016/j.corsci.2019.05.029.

[11] R.B. Rebak, V.K. Gupta, M. Larsen, Oxidation characteristics of two FeCrAl alloys in air and steam from 800 °C to 1300 °C, JOM 70 (2018) 1484–1492, doi:10.1007/s11837-018-2979-9.

[12] C. Kim, H. Kim, W. Heo, C. Jang, S.Y. Lee, S. Lee, J.-.S. Lee, High-temperature steam oxidation behavior of alumina-forming duplex FeNiCrAl and ferritic FeCrAl alloys at 800 °C to 1050 °C, Corros. Sci. 190 (2021) 109658, doi:10.1016/j.corsci.2021.109658.

[13] S. Dryepndt, K.A. Unocic, D.T. Hoelzer, C.P. Massey, B.A. Pint, Development of low-Cr ODS FeCrAl alloys for accident-tolerant fuel cladding, J. Nucl. Mater. 501 (2018) 59–71, doi:10.1016/j.jnucmat.2017.12.035.

[14] I. Gurrappa, S. Weinbruch, D. Naumenko, W.J. Quadakkers, Factors governing breakaway oxidation of FeCrAl-based alloys, Mater. Corros. 51 (2000) 224–235, doi:10.1002/(SICI)1521-4176(200004)51:4⟨224::AID-MACO224⟩3.0.CO;2-B.

[15] Z. Sun, Y. Yamamoto, Processability evaluation of a Mo-containing FeCrAl alloy for seamless thin-wall tube fabrication, Mater. Sci. Eng. A 700 (2017) 554–561, doi:10.1016/j.msea.2017.06.036.

[16] M. Steinbrück, N. Vér, M. Große, Oxidation of advanced zirconium cladding alloys in steam at temperatures in the range of 600-1200 °C, Oxid. Met. 76 (2011) 215–232, doi:10.1007/s11085-011-9249-3.

[17] J.W. McMurray, R. Hu, S.V. Ushakov, D. Shin, B.A. Pint, K.A. Terrani, A. Navrotsky, Solid-liquid phase equilibria of Fe-Cr-Al alloys and spinels, J. Nucl. Mater. 492 (2017) 128–133, doi:10.1016/j.jnucmat.2017.05.016.

[18] B.A. Pint, K.A. Terrani, Y. Yamamoto, L.L. Snead, Material selection for accident tolerant fuel cladding, Metall. Mater. Trans. E 2 (2015) 190–196, doi:10.1007/s40553-015-0056-7.

[19] G.C. Rybicki, J.L. Smialek, Effect of the θ-α-Al_2O_3 transformation on the oxidation behavior of β-NiAl + Zr, Oxid. Met. 31 (3/4) (1989) 275–304, doi:10.1007/BF00846690.

[20] A.T. Nelson, E.S. Sooby, Y.-.J. Kim, B. Cheng, S.A. Maloy, High temperature oxidation of molybdenum in water vapor environments, J. Nucl. Mater. 448 (2014) 441–447, doi:10.1016/j.jnucmat.2013.10.043.

[21] C.D. Versteylen, N.H. van Dijk, M.H.F. Sluiter, First-principles analysis of solute diffusion in dilute bcc Fe-X alloys, Phys. Rev. B 96 (2017) 094105, doi:10.1103/PhysRevB.96.094105.

[22] H. Josefsson, F. Liu, J.-.E. Svensson, M. Halvarsson, L.-.G. Johansson, Oxidation of FeCrAl alloys at 500-900 °C in dry O_2, Mater. Corros. 56 (11) (2005) 801–805, doi:10.1002/maco.200503882.

[23] K.A. Kane, S.K. Lee, S.B. Bell, N.R. Brown, B.A. Pint, Burst behavior of nuclear grade FeCrAl and Zircaloy-2 fuel cladding under simulated cyclic dry out conditions, J. Nucl. Mater. 539 (2020) 152256, doi:10.1016/j.jnumat.2020.152256.

[24] R. Chegroune, E. Salhi, A. Crisci, Y. Wouters, A. Galerie, On the competitive growth of alpha and transient aluminas during the first stages of thermal oxidation of FeCrAl alloys at intermediate temperatures, Oxid. Met. 70 (2008) 331–337, doi:10.1007/s11085-008-9126-x.

[25] W.J. Quadakkers, H. Holzbrecher, K.G. Briefs, H. Beske, Differences in growth mechanisms of oxide scales formed on ODS and conventional wrought alloys, Oxid. Met. 32 (1/2) (1989) 67–88, doi:10.1007/BF00665269.

[26] S. Dryepondt, B.A. Pint, Effect of Fe-Al substrate mechanical properties on alumina scale morphology, Mater. Sci. and Eng. A 497 (2008) 224–230, doi:10.1016/j.msea.2008.07.005.

[27] T. Maeda, S. Ukai, S. Hayashi, N. Oono, Y. Shizukawa, K. Sakamoto, Effect of zirconium and oxygen on the oxidation of FeCrAl-ODS alloys under air and steam conditions up to 1500 °C, J. Nucl. Mater. 516 (2019) 317–326, doi:10.1016/j.jnucmat.2019.01.041.

[28] K. Lipkina, D. Hallatt, E. Geiger, B.W.N. Fitzpatrick, K. Sakamoto, H. Shibata, M.H.A. Piro, A study of the oxidation behaviour of FeCrAl-ODS in air and steam environments up to 1400 °C, J. Nucl. Mater. 541 (2020) 152305, doi:10.1016/j.jnucmat.2020.152305.

[29] T. Kaito, T. Narita, S. Ukai, Y. Matsuda, High temperature oxidation behavior of ODS steels, J. Nucl. Mater. 329-333 (2004) 1388–1392, doi:10.1016/j.jnucmat.2004.04.203.

[30] S.B. Bell, K.A. Kane, C.P. Massey, L.A. Baldesberger, D. Lutz, B.A. Pint, Strength and rupture geometry of un-irradiated C26M FeCrAl under LOCA burst testing conditions, J. Nucl. Mater. 557 (2021) 153242, doi:10.1016/j.jnucmat.2021.153242.